Master Thesis

Impact of Surface Terminations on NV Center Surface Interactions and Optical Charge-State Dynamics

Author:
Patrik Tognina

Supervisors:
Beat Bürgler
Tobias Sjölander
Patrick Maletinsky

University of Basel
Quantum Sensing Lab

November 12, 2024

Nitrogen-Vacancy (NV) centers in diamond are highly versatile quantum sensors, capable of probing magnetic fields on the nanoscale and offering unique opportunities for high-sensitivity nuclear magnetic resonance (NMR) spectroscopy. Charge state stability of NV^- is crucial for its sensing capabilities, yet it is strongly influenced by surface chemistry. Here we demonstrate the successful optical charge-state conversion of NV centers (from neutral to negatively charged) after deuterium (D_2) termination with a 515 nm laser. We postulate that this process is accompanied by a gradual replacement of the D_2 termination with a mixture of oxygen and hydroxyl groups due to surface oxidation. Optical properties, such as optically detected magnetic resonance (ODMR) contrast and signal-to-noise ratio (SNR), were investigated in NV centers located in diamond pillars with the surface after charge-state conversion and compared to those with an oxygen-terminated surface where we find greater ODMR contrast and SNR on an oxygen terminated surface. We also investigate the role of different diamond surface treatments— tri-acid cleaned, and the surface resulting from D_2 termination followed by charge-state conversion— on surface-bound hydrogen using Spin-Lock NMR. A persistent hydrogen NMR signal was detected on both surfaces while we report an increased hydrogen signal strength after D_2 termination and charge-state conversion.

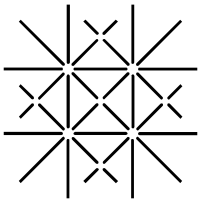

Contents

1 Motivation

The nitrogen-vacancy (NV) center [1], a defect within the diamond lattice, is a focal point of quantum research due to its unique properties. It contains a solid-state spin that exhibits long coherence times at room temperature [2] and can be controlled both optically with green light, enabling optical spin initialization and readout, and magnetically with radio frequency microwaves, allowing for coherent spin manipulation. These properties make the NV center an ideal candidate for use in quantum technologies, like quantum computing, magnetometry and nanoscale sensing, offering a pathway to stable, high-resolution sensors [3]. Shallow NV centers, located close to the diamond surface, are particularly advantageous for nanoscale sensing applications such as scanning probe magnetometry [4] and nuclear magnetic resonance (NMR) spectroscopy [5] since their proximity to the external field source enhances both the strength of signals of interest and the spatial resolution [6]. This close interaction with surface signals also allows for the detection of weak magnetic fields, making shallow NVs ideal for high-sensitivity applications, such as detecting single nuclear spins or imaging at the nanoscale.
However, the surface chemistry of diamond presents a significant challenge for sensing applications. Surface spins can drastically reduce coherence times of NV's - in particular shallow ones - limiting their performance in quantum experiments [6]. Additionally, specific surface terminations can introduce unwanted nuclear spins that contaminate NMR spectra. Surface chemistry also directly affects the NV charge state [7], where certain terminations can act as electron donors or acceptors, influencing whether the NV center is in its negatively charged state (NV^-) or its neutral state (NV^0). The stability of the NV^- charge state is crucial for effective quantum sensing, and thus, the surface composition and charge dynamics must be carefully controlled.
Interestingly, we observe a hydrogen Nuclear Magnetic Resonance (NMR) spectroscopy signal (Larmor frequency of protons) on an oxygen-terminated diamond surface. This signal persists even in the absence of external hydrogen sources, such as immersion oil. It is assumed that this signal originates from hydrogen-containing species directly bound to the diamond surface, such as hydroxyl (OH) groups [8]. However, the precise origin of this signal remains uncertain.
To further investigate this hydrogen signal, we terminate the diamond with deuterium (D_2), replacing potential hydrogen-containing species on the surface with D_2. This approach allows us to test whether the detected hydrogen signal is attributable to hydrogen bonds on the surface of the diamond.
After D_2 termination, the NV centers predominantly occupy the neutral NV^0 charge state due to the altered surface chemistry. To restore the NV centers to the negatively charged NV^- state, which is essential for optimal sensing, we perform a charge-state conversion process using continued 515 nm laser illumination. Through Spin-Lock NMR spectroscopy, we examine the hydrogen signal on oxygen-terminated diamond and compare the results with those obtained after D_2 termination and successful charge state conversion. These investigations provide valuable insights into how different surface chemistry's influence the NV charge state and the nature of the hydrogen NMR signals.

2 Theoretical Background

In this section, we present the fundamental physical concepts relevant to the experiments performed in this thesis. We begin with an introduction to the NV center in diamond, accompanied by a quantum mechanical description of its electronic structure (energy levels) in Sec 2.1. Subsequently, Sec 2.2 elaborates on the optical driving of the NV center, which enables spin initialization and readout. Sec 4.1 addresses the NV charge-state conversion process, detailing the conversion from NV^0 to NV^- and the influence of different surface terminations on the NV charge state. The coherent manipulation of a two-level spin system using microwave fields is explored later in Sec 5.1. Sections Sec 5.2 and Sec 5.3 then delve into the Spin-Lock sequence and the impact of environmental noise on spin dynamics.

2.1 Electronic Energy Levels Of The Nitrogen-Vacancy Center

The NV center [1] is a defect in the diamond lattice that consists of a substitutional nitrogen atom (N) located next to a vacant carbon site (V), as shown in Fig. 1 (A). While this defect can exist in multiple charge states, only the NV^- and NV^0 are of interest for this thesis. The NV^- state consists of six electrons where the additional electron compared to NV^0 is typically donated by surrounding dopants or impurities within the diamond.

In the negatively charged state, the NV center behaves as a spin $S = 1$ in its electronic ground state, leading to three distinct spin eigenstates with magnetic quantum numbers $m_S \in \{0, \pm 1\}$, aligned onto the NV center's symmetry axis. These spin states are labeled as $|0\rangle$, $|1\rangle$, and $|-1\rangle$. Due to spin-spin interactions, the $|0\rangle$ state is separated from the $|\pm 1\rangle$ states by the zero-field splitting $D_{\text{gs}} = 2\pi \times 2.87\text{GHz}$, as illustrated in Fig. 1 (B). The $m_S = \pm 1$ states are degenerate unless an external magnetic field is applied. When a static magnetic field B_z is applied along the NV symmetry axis, it induces a Zeeman splitting between the $m_S = \pm 1$ states. The energy difference is expressed as $\Delta E = 2\gamma_{\text{NV}} B_z$, where $\gamma_{\text{NV}} = g_e \mu_B = 2\pi \times 2.79\text{MHz/G}$ [1]. Here, $g_e \approx 2$ is the electron g-factor, and μ_B is the Bohr magneton. In addition to the Zeeman splitting, the NV center's electronic spin states are also split due to hyperfine interactions with the nitrogen nucleus. For this study, the focus is exclusively on NV's formed by the isotope ^{14}N, which has a nuclear spin $I = 1$ Fig. 1 (B). The hyperfine interaction results in a further splitting of the NV spin states based on the nuclear spin projections $m_I \in \{0, \pm 1\}$ onto the NV quantization axis. Finally, there is a nuclear Zeeman effect which, due to its relatively small nuclear gyromagnetic ratio ($\gamma_{N_{14}} = 2\pi \times 0.3\text{kHz/G}$ [9]), is negligible compared to the electronic spin interactions and is thus omitted from the ground-state Hamiltonian $\hat{H}_{\text{gs}}$ that is given by Eq. (1) ([10]).

$$\mathcal{H}_{\text{gs}} = \hbar \cdot \left(\underbrace{D_{\text{gs}} \hat{S}_z^2 \otimes \hat{I}_0}_{\text{fine structure}} + \underbrace{\gamma_{NV} B_z \hat{S}_z \otimes \hat{I}_0}_{\text{Zeeman splitting}} + \underbrace{P \hat{S}_0 \otimes \hat{I}_2^2 + A_{\text{gs}}^{\parallel} \hat{S}_z \otimes \hat{I}_z + A_{\text{gs}}^{\perp} \left(\hat{S}_x \otimes \hat{I}_x + \hat{S}_y \otimes \hat{I}_y \right)}_{\text{hyperfine structure}} \right), \quad (1)$$

Here, $S_{x,y,z}$ denote the NV spin operators, $\hat{I}_{x,y,z}$ the nuclear spin operators, and S_0 and I_0 the respective unity operators. $P = -2\pi \times 4.95\text{MHz}$ represents the nuclear electric quadrupole coupling parameter [11], and $A_{gs}^{\parallel} = -2\pi \times 2.17\text{MHz}$ and $A_{gs}^{\perp} = -2\pi \times 2.7\text{MHz}$ represent the axial and transverse magnetic hyperfine parameters, respectively [12]. These hyperfine interactions further split the energy levels of the system also shown in Fig. 1, where $|m_S, m_I\rangle$ denotes the combined electronic and nuclear spin states.

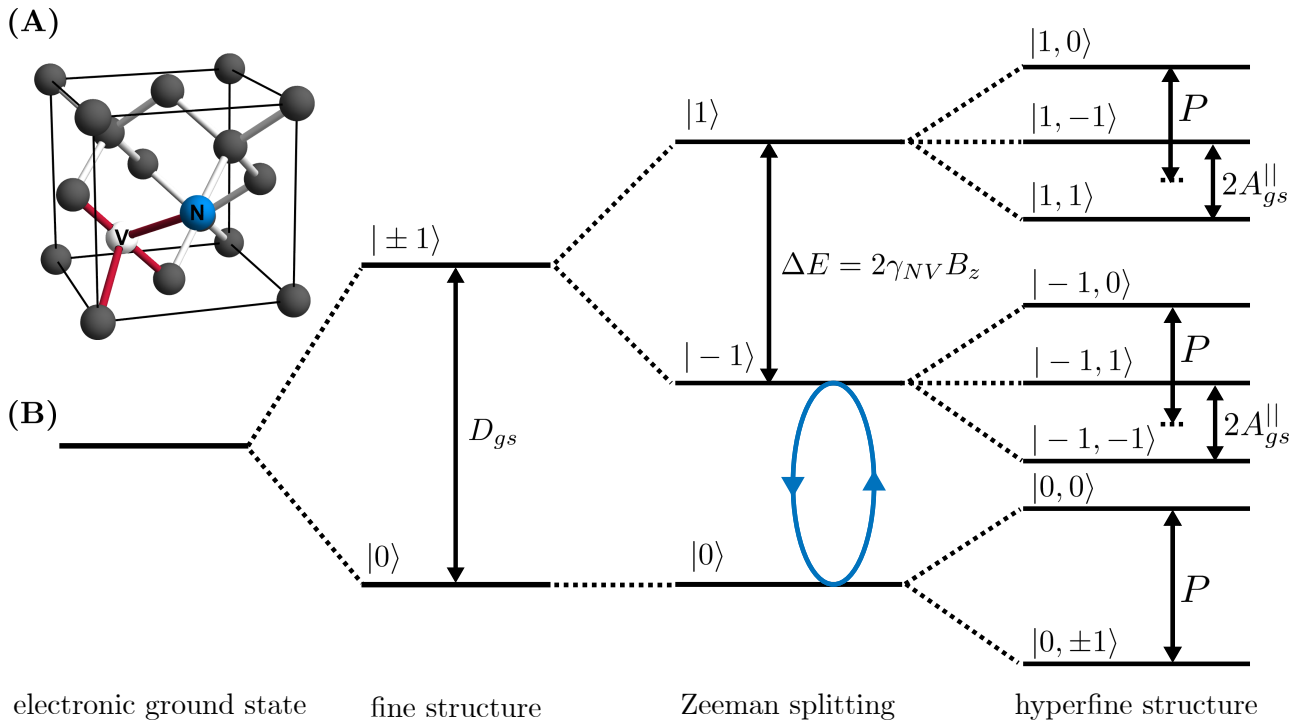

Figure 1: (A) Crystal structure of the NV center with the substitutional nitrogen atom (blue) and the vacancy (white). The lattice structure is a face-centered cubic lattice with two carbon atoms per unit cell (grey). **(B)** Energy levels of the NV center's ground state (not to scale), taking into account the fine structure, Zeeman splitting, and the hyperfine structure. Coherent spin manipulations of the two-level system, composed of $|0\rangle$ and $|-1\rangle$ states, can be achieved using a transverse microwave (MW) field (blue) characterized by the Rabi frequency Ω_R which is directly proportional to the strength of the applied MW field. (Figure adapted from [10])

2.2 Optical Spin Initialization And Readout

The nitrogen-vacancy (NV) center can be optically excited by targeting the electronic transition between its ground and excited states. When illuminated with green laser light, the population in the ground state is non-resonantly promoted to vibrational levels with energies above the excited state. These excited states are then populated through non-radiative, phonon-mediated processes which move the population from the vibrational states to the excited state. Following this, the excited state population decays back to the ground state, emitting photons in a process known as photoluminescence (PL). The light emitted in this process corresponds to red light with a wavelength of 637 nm, representing the zero-phonon line in the emission spectrum [1]. Both optical excitation and the subsequent decay preserve the spin state, meaning that the magnetic quantum number m_S remains the same.

Between the ground and excited states, there are also metastable singlet states [1]. These singlet states can be populated from the excited state, after which the population predominantly relaxes back to the $m_S = 0$ state in the ground state manifold. Consequently, continuous illumination with green laser light polarizes the NV center's spin into the $|0\rangle$ state via spin-selective relaxation through the singlet states.

with transitions to the singlets being more probable for the $m_S = \pm 1$ spin states compared to the $m_S = 0$ state, these states exhibit lower PL intensity compared to the $m_S = 0$ state. This spin-dependent difference in PL intensity, enables the optical readout of the NV center's spin state.

3 Measurement Setup

The data presented in this thesis was acquired using a previously completed home-built confocal microscope system designed for spin manipulation experiments at room temperature. A detailed schematic of the setup is shown in Fig. 2. This setup allows precise optical control and detection of NV center spin states using laser and microwave components for spin initialization, manipulation, and readout.
The system employs optical spin initialization (shown in green) and photoluminescence (PL) detection (shown in red) through a confocal microscope system. A 515 nm green laser (Cobolt 06-MLD) is focused onto the NV centers in the diamond sample via an optical objective (Olympus LMPLFLN100x). The emitted red PL from the NV centers is collected through the same objective and subsequently coupled into an optical fiber, routed to an avalanche photodiode (APD) for photon detection. To separate the excitation laser and the emitted PL, a dichroic beamsplitter is used, which reflects the green laser while transmitting the red PL, ensuring that only the desired wavelengths reach the APD. To achieve precise timing control of the laser and the APD counter, a pulse blaster is employed. This device coordinates the timing of the laser and collecting windows. The pulse blaster is also connected to the AWG, serving as a trigger signal to ensure accurate synchronization for spin initialization, microwave manipulation, and readout sequences.
The laser path includes an acousto-optic modulator (AOM, Crystal Technology Inc. 3200-146 30581), which is connected to the pulse blaster. The AOM allows for rapid, precise control of laser power and pulse duration during the experiments.
A piezo-controlled stage (Dyneos P-517.3CD) is used to position the microscope objective, providing fine control over the focus of the laser spot on the diamond sample. This enables high-precision spatial mapping of NV centers and ensures optimal focusing during experiments.
Microwave (MW) control (depicted in blue) is achieved through an IQ mixer (Polyphase Microwaves 2874), which modulates MW signals using inputs from both an arbitrary waveform generator (Tektronix AWG5014C) and a Rohde und Schwarz, R&S (SMB 100A) MW generator. The IQ mixer allows independent control of the phase and amplitude of the MW signal. By controlling the inputs to the I and Q channels, a 90-degree phase shift between MW pulses can be generated, a key requirement for Spin-Locking protocols, see Sec 5.3. The modulated MW signal is amplified (Agilent E3644A) and then delivered to the diamond sample via a loop gold wire positioned near the diamond. A Keysight waveform generator (33500B series) produces two calibration signals, which are applied through a second wire positioned near the diamond sample. These signals serve as reference points for calibration during a Spin-Lock experiment.
Many experiments in this thesis are performed near the excited state level anti-crossing (ESLAC) in diamond [13], occurring at an external magnetic field of approximately 512 G along the NV axis. At this field, resonant coupling between the NV electronic spin and the ^{14}N nuclear spin is facilitated through spin flip-flop processes in the NV's excited state. Optical pumping near the ESLAC polarizes the ^{14}N nuclear spin into a single spin state, effectively trapping the spin population in one of the hyperfine states. This results in enhanced signal-to-noise ratio and ensures resonant driving conditions for microwaves, avoiding off-resonant transitions that could disrupt measurements. The hyperfine polarization at the ESLAC is robust, maintaining its effectiveness even at magnetic fields deviating up to 150G from the exact ESLAC condition [14]. For these reasons, the magnetic field in our experiments is set to $B_z \approx 512$ G where the ESLAC occurs, optimizing the conditions for nuclear spin-based sensing and signal readout. This specific field strength is achived by placing a permanent neodynium magnet (supermagnete.ch: CN-25-13-10-N) in close proximity to the diamond sample. The magnetic field alignment with the NV axis is adjusted using a millimeter piezo stick-slip x-y-z-stage from SmarAct (XYZ-SLC1730).

Experiments were conducted on several NV centers within the same diamond sample. The diamond sample was prepared by nitrogen ion implantation (implantation energy: 12keV, implantation angle: 7°), followed by high-temperature annealing to form NV centers. After annealing, parabolic pillar structures were etched into the diamond surface to improve the collection efficiency of the PL signal through optical waveguiding [15]. This enhanced PL collection allowed for more reliable detection of single NV centers and improved the signal-to-noise ratio in measurements.
Additionally, these pillar structures enable us to locate the same NV on the diamond for different measure-

ment series.

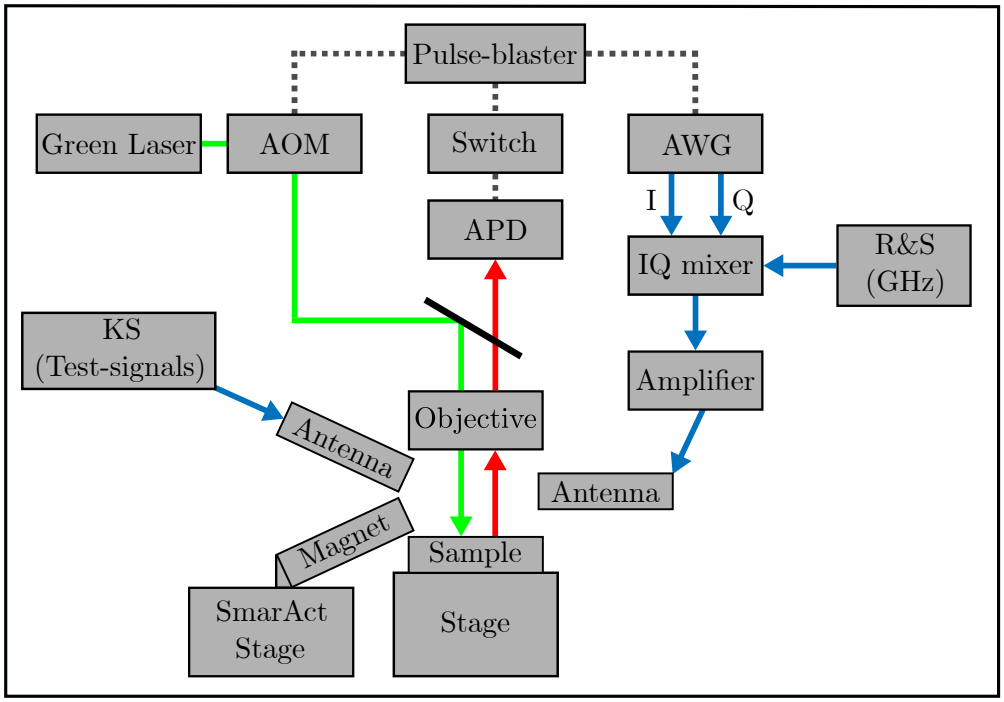

Figure 2: Schematic of the experimental setup. The setup includes a confocal microscope, using a green laser for both optical initialization and readout, with an avalanche photodiode (APD) for collection. The microwave (MW) signal generation (blue path) is achieved using an IQ mixer that combines the MW from the Rohde und Schwarz (R&S) and the signals from the I and Q channels of an arbitrary waveform generator (AWG). The MW signal is amplified and applied to the sample through a loop gold antenna. A Keysight waveform generator produces two calibration-signals which are applied through a second antenna. The sample is exposed to a static magnetic field generated by a permanent magnet, which is precisely positioned using a SmarAct stage. The entire setup is controlled and synchronized via a pulse-blaster. The sample is placed on a manual micrometer stage (Newport M-562 series) that allows for fine adjustments of its position relative to the MW and laser paths.

4 Laser Assisted Charge-State Control Of NV Centers

4.1 Charge-State Control Of The NV Center's In Diamond

Shallow NV^- centers close to the diamond surface tend to lose their charge when the surface is hydrogen-terminated, resulting in a dominant appearance of the NV^0 charge state over NV^-. This phenomenon is attributed to the surface band bending induced by the hydrogen termination [7]. Importantly, we observed a similar shift in the charge state distribution following deuterium (D_2) termination. This observation underscores that deuterium termination induces comparable band bending effects as hydrogen, resulting in a similar destabilization of the NV^- state. Given that the surface chemistry of deuterium and hydrogen terminations are expected to be similar, this observation is expected, however, it has not been previously reported. The choice of D_2 termination was made to facilitate our investigation into the hydrogen NMR signal detected on oxygen-terminated diamond, as discussed in Sec. 1.

The type of surface termination directly affects the band bending of diamond by altering the electron affinity, χ, of the surface, which in turn influences the positions of the valence and conduction bands as well as the charge transition levels relative to the Fermi level (E_F) in the diamond. For example, hydrogen-terminated diamond surfaces exhibit a negative electron affinity ($\chi = -1.3 \pm 0.1$ eV) [16], leading to upward band bending of the valence and conduction bands, which can cause the NV^0/NV^- charge transition level to cross E_F, thereby stabilizing the NV^0 charge state. The band bending is caused by the formation of a p-type surface layer on hydrogen terminated diamond [17]. When exposed to air, the diamond surface attracts a layer of atmospheric adsorbates enabling electron transfer from the diamond to this layer resulting in a depletion of electrons and an accumulation of holes near the diamond surface. This p-type layer causes the band bending, making the neutral NV^0 state dominant compared to the NV^- state.

Moreover, the findings presented in [18] suggest that the charge state of defects in diamond is strongly influenced by their local environment, particularly their proximity to nitrogen donors, rather than the global position of the Fermi level. Defects near nitrogen donors are more likely to be in negative charge states, while those farther away may remain neutral. This proximity effect explains why color centers in diamond can exist in different charge states even within the same crystal. Therefore, at high nitrogen concentrations in the host lattice, the NV center is more likely to be in the NV^- state.

Continuous illumination of the sample with a laser can alter the surface properties of diamond [19]. Specifically, illumination can restore the NV^- charge state following hydrogen or deuterium surface termination. This process is observed as a gradual increase in photoluminescence (PL) and enhanced contrast in optically detected magnetic resonance (ODMR) experiments. We demonstrate the possible charge-state conversion of NV center on deuterium terminated diamond, both within pillar structures and on bulk diamond using a 515 nm laser at powers between 500μW-2mW.

Kaviani et al. [16] and Zuber [8] suggest that during illumination the termination gets replaced by mostly hydroxyl groups (OH) and C-O-C bonds, creating the suggested ideal surface in [16] for NV^- stability. The surface evolution is illustrated in Fig. 3. In the following, the surface resulting from a tri-acid cleaning process is referred to as the oxygen terminated surface, the surface after terminating the diamond with deuterium as the deuterium surface and the surface after D_2 termination and charge-state conversion as the converted surface. How exactly the oxygen terminated surface and the converted surface look like is not fully determined and subject of investigation.

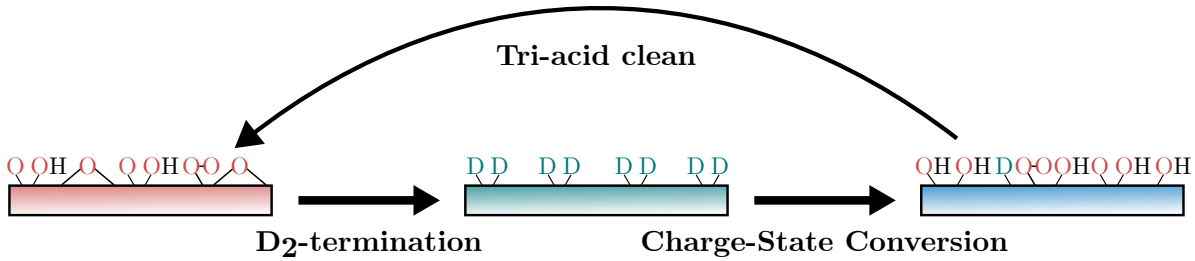

Figure 3: Evolution of the diamond surface through the different stages. **Left:** After an try-acid clean the diamond is oxygen terminated. **Middle:** Deuterium terminated surface. **Right:** Surface after Deuterium termination and charge-state conversion, called the *converted surface* in the following. (Note that these illustrations of the surfaces are based on the hypothesis in this thesis)

4.2 Demostration Of NV Charge-State Conversion In Diamond Pillars and on Bulk Diamond

We demonstrate the successful optical charge-state conversion of the NV center on both diamond pillars and bulk diamond. Fig. 4 presents the successful conversion of an NV center's charge state within a diamond pillar. The curves in Fig. 4 (C) were obtained by measuring the photoluminescence (PL) intensity over time while continuously illuminating the NV centers with a laser power of 500µW. During this process, for every 10% increase in PL intensity, an ODMR measurement was performed at a standard laser power of 50µW. The evolution of the PL intensity over time reflects a continuous process where the surface termination evolves, where D_2 is progressively being replaced by predominantly oxygen and hydroxyl groups. The resulting surface termination modifies the local band bending, altering charge-state distribution, ultimately favoring NV^- over NV^0. Initially, following deuterium termination, the PL intensity is dominated by NV centers in the NV^0 state, as revealed by the absence of distinct ODMR features. The curve depicted in Fig. 4 (C) shows a distinct trend, characterized by an initial plateau of constant low PL followed by a sharp increase until reaching a PL peak, followed by a gradual decline to a steady state. The time-scales of this conversion are vastly different between different NV's but show all the same characteristic shape. This conversion of the NV's charge state has also been observed in bulk diamond, Fig. 6.
The ODMR data obtained during the revival process indicate that substantial ODMR contrast only starts to appear after the PL had reached its steady state. It should be noted that no ODMR data was acquired at the PL peak and immediately afterward, until the PL plateau was reached. This limitation is due how the measurement was setup. As $NV^-$is the brightest charge state of the defect [1], we expect that the peak in PL and the peak in ODMR contrast coincide, which is clearly not the case, as shown in Fig. 4 (C).

One can speculate about potential issues with measuring ODMR contrast at the PL peak and the PL drop towards the PL plateau. One possible explanation for the observed drop in PL intensity toward the plateau after reaching the initial PL peak, is a variation in the background PL response due to changes in surface conditions during the charge-state conversion process. The PL curve over time, shown in Fig. 4 (C), reflects a combination of both the NV center PL signal and background PL contributions. Any temporal fluctuations in the background PL during this conversion would imply that the isolated NV PL signal differs from the observed curve. One possible cause of the changing background PL is that tightly focused high power (0.5-2mW) laser we apply here acts as an optical tweezer and attracts "dirt" from the environment which gets deposited on the diamond surface, causing an initial rise in PL. Continued illumination would then photo-bleach these deposits, causing a decline in PL, [20].

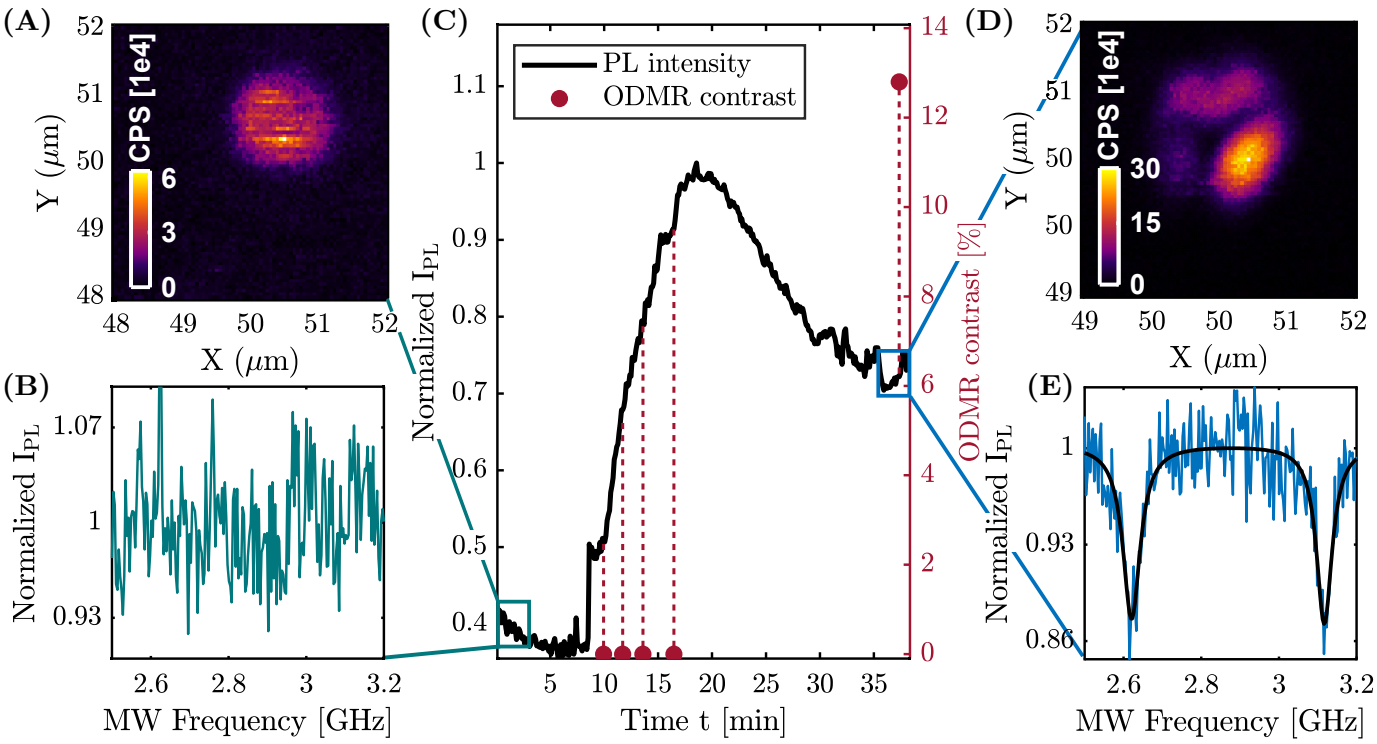

Figure 4: **(A)** PL scan of a pillar in diamond directly after D_2 termination. **(B)** ODMR measurement on the pillar directly after D_2 termination at 50 µW laser power. No ODMR signature is observed. **(C)** PL as a function of time during 515 nm laser illumination on pillar (black). The data is normalized to the maximal PL intensity measured. The red dots display the ODMR contrast. The dotted red lines mark where on the PL time trace these measurements took place. **(D)** PL scan of the same pillar in diamond after laser assisted charge-state conversion. **(E)** ODMR measurement on the same pillar directly after laser assisted charge-state conversion at 50μW laser power, showing the NV^- ODMR signature. The black line is a gaussian fit.

To investigate this hypothesis a spectral analysis was conducted throughout the charge-state conversion process, Fig. 5. Unlike the behavior observed in previous measurements where the PL exhibited a peak followed by a decrease towards a stable plateau (Fig. 4 (C)), the PL in Fig. 5 (A) continuously increased until reaching a stable, saturated state. This discrepancy from the previously observed PL dynamics may be attributed to the substantially lower laser power used during this measurement (200 µW). At this lower laser power, the laser may be less effective at attracting and depositing "dirt" onto the diamond surface, thereby eliminating the characteristic initial PL peak and subsequent decline associated with photo-bleaching of surface contaminants.

The ODMR contrast, plotted alongside the PL, reveals a gradual increase throughout the charge-state conversion process. This behavior is likely a consequence of the experimental protocol, wherein ODMR measurements were performed with a higher number of repetitions, making it possible to observe even low-contrast ODMR features and capturing the gradual emergence of a stable NV^- state.

To quantify the contributions of the two different charge states NV^0 and NV^- during the conversion process, PL spectra were recorded at regular intervals. An initial spectrum was acquired to characterize the NV^0 charge-state distribution, followed by a final spectrum (after PL has reached a stable regime) to capture the contribution of NV^-, Fig. 5 (C). Each other spectrum taken in between was individually fitted as a superposition of these two reference spectra for NV^0 and NV^-, determining of the relative contributions of each charge state to the overall spectrum. The temporal evolution of these contributions is depicted in panel Fig. 5 (B), illustrating the progressive conversion from NV^0 to NV^-.

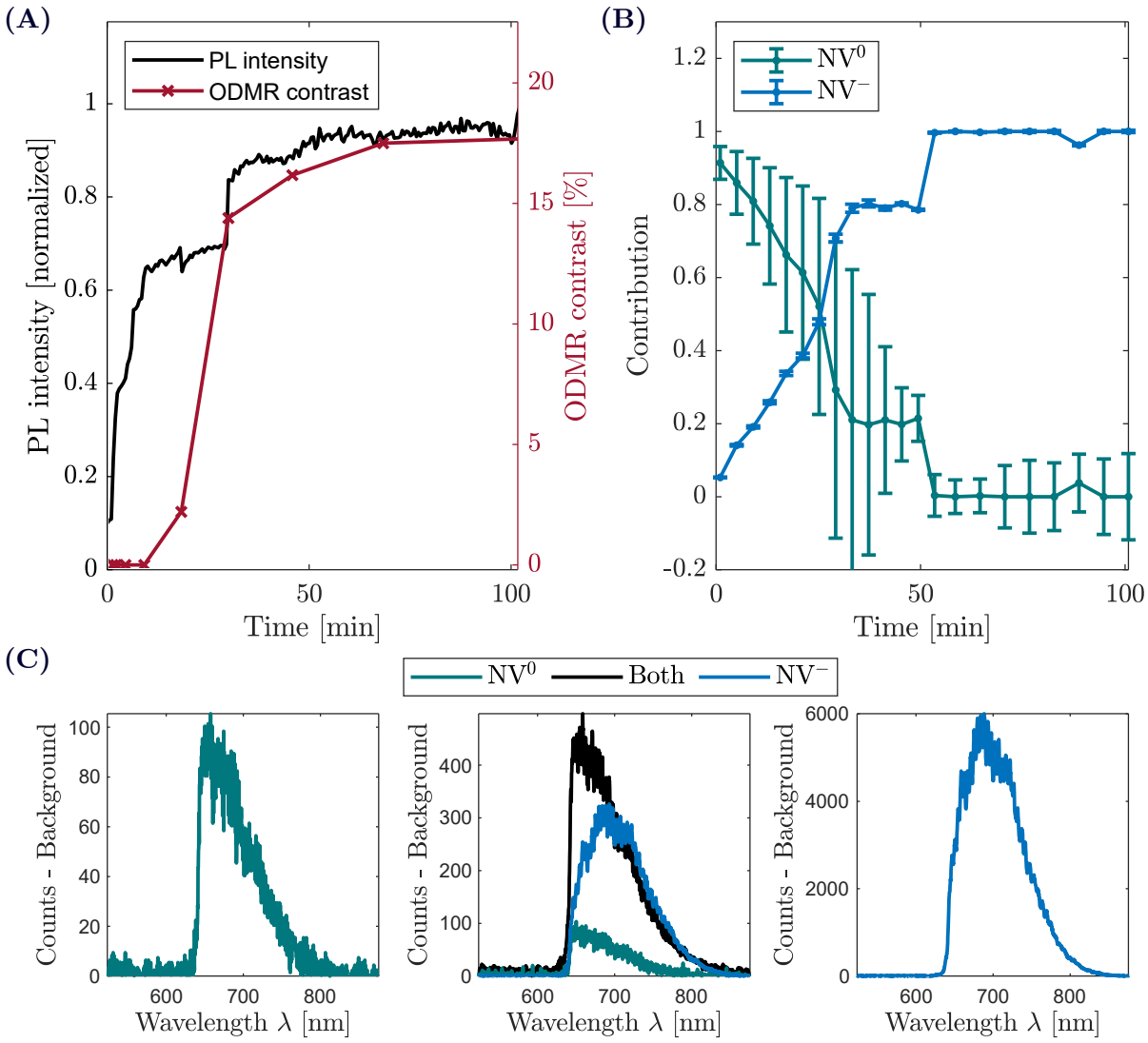

Figure 5: **(A)** PL as a function of time during 515 nm laser illumination on pillar (black). The data is normalized to the maximal PL intensity measured. The red line displays the ODMR contrast as a function of time. **(B)** Fitted contributions of NV^0 (green) and NV^- (blue) as a function of time during the charge-state conversion process. The bars display the fit errors. **(C)** Examples of spectra during the charge-state conversion process. Left: Initial spectrum used to fit the NV^0 contribution. Middle: Spectrum during charge-state conversion process (black) with the fitted contributions of NV^0 (green) and NV^- (blue). Right: Final spectrum used to fit the NV^- contribution.

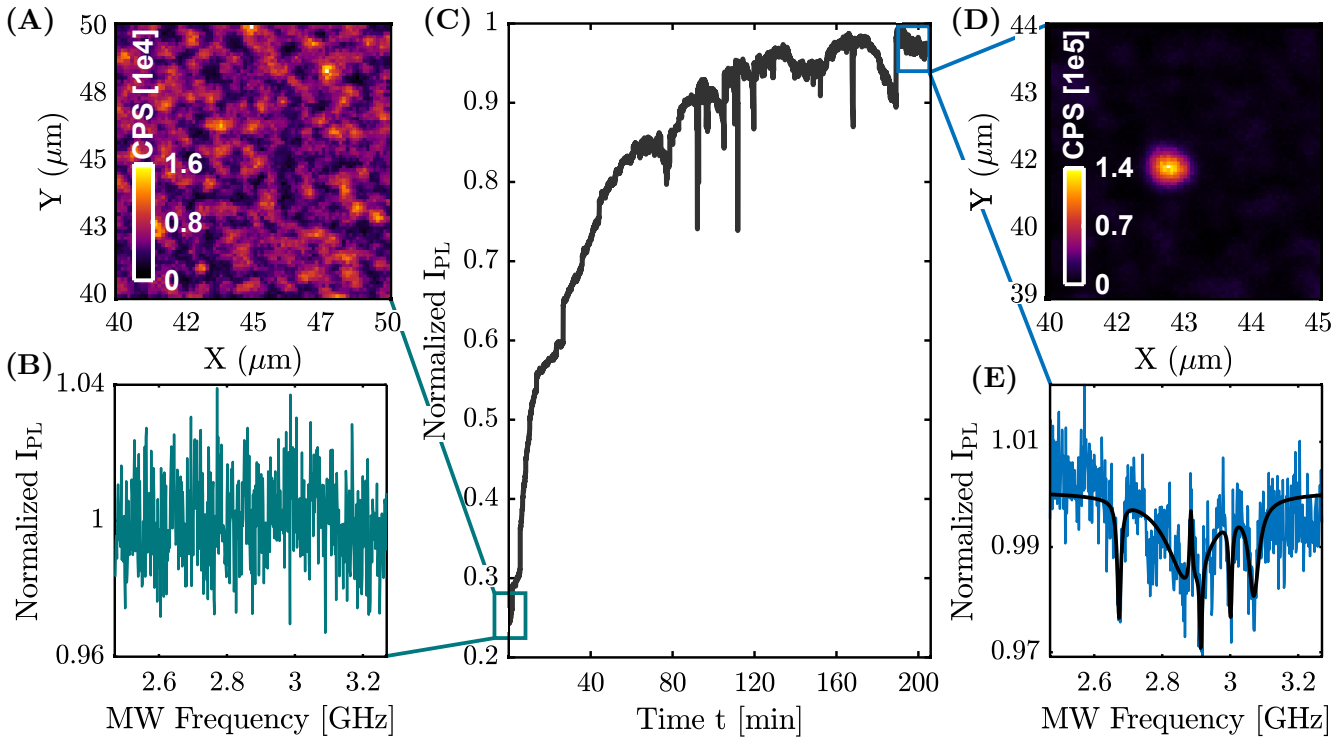

Figure 6: **(A)** PL scan on bulk diamond directly after D_2 termination. **(B)** ODMR measurement on bulk diamond directly after D_2 termination at 50μW laser power. No ODMR signature is observed. **(C)** PL as a function of time during 515 nm laser illumination on pillars, normalized to the maximal PL intensity measured (black). **(D)** PL scan on bulk diamond after laser assisted charge-state conversion. **(E)** ODMR measurement on bulk diamond directly after laser assisted charge-state conversion at 50μW laser power, showing the NV^- ODMR signature. The black line is a gaussian fit.

Extending the experiment shown in Fig. 4 (C) to even longer times, we find that continuous laser illumination further enhanced the performance of the NV centers, resulting in a noticeable increase in both ODMR contrast and Signal-to-Noise Ratio (SNR). The SNR in an ODMR type experiment is defined as the ratio of the contrast and the standard deviation (STD) of the PL data. As shown in Fig. 7, both SNR (blue line) and the contrast (red line) demonstrated a progressive increase over time during this extended illumination period, while the STD, depicted in the inset (grey), shows some fluctuations but no significant in- or decrease after the 16 hours. This stable behavior of the STD suggests that the observed rise in SNR is predominantly driven by an increase in contrast rather than a reduction in noise levels.

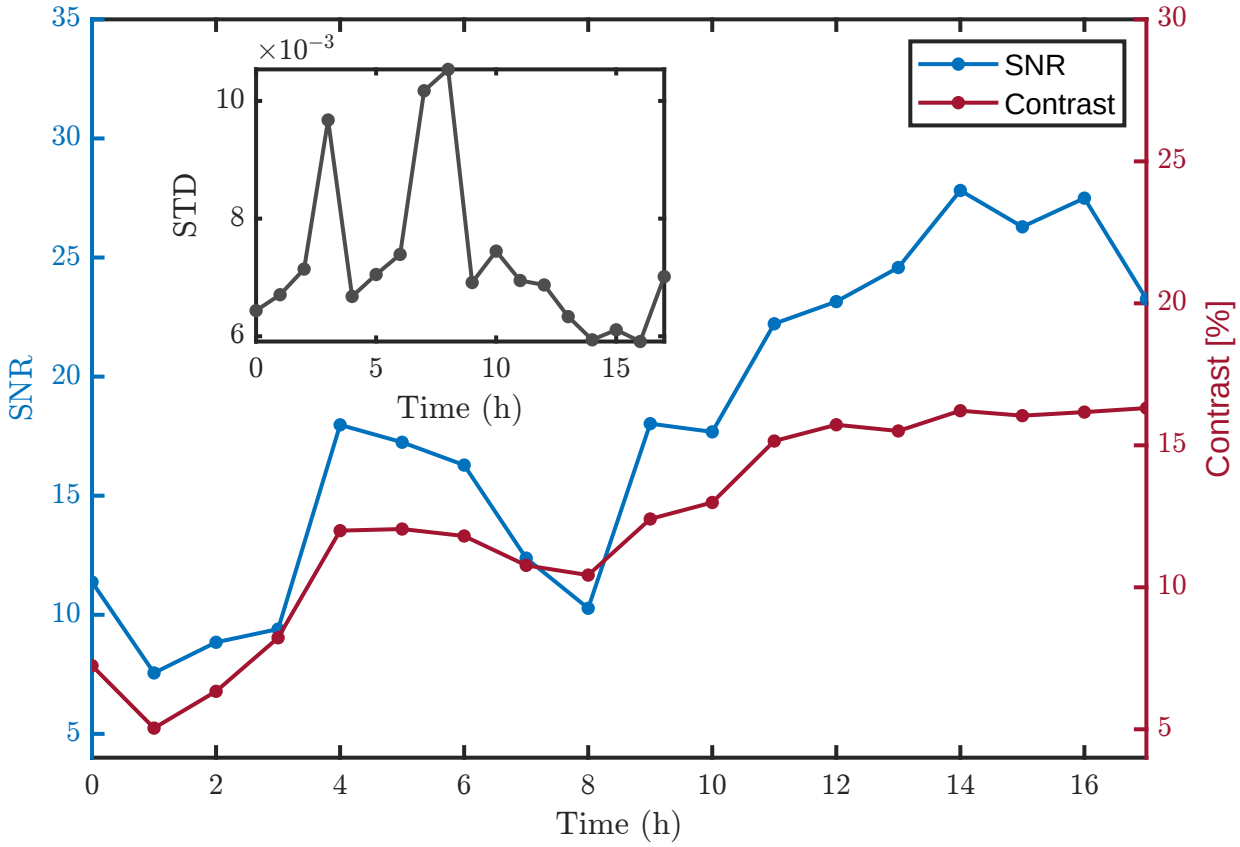

Figure 7: Evolution of the ODMR contrast and SNR over time during continued laser illumination after successful charge-state conversion. The blue line represents the SNR (left y-axis), the red line the contrast (right y-axis). The inset displays the standard deviation (STD) over time, indicating that the increase in SNR is primarily driven by the increase in contrast, while the STD remains relatively stable.

4.3 Charge-State Conversion Statistics

The time required for the NV charge-state conversion process varies greatly across different diamond pillars. Fig. 8 (A) shows the conversion time, the time it takes to reach the stable PL regime after the PL peak and the laser power applied during the process (legend). It is evident from the figure that there is significant variability in the conversion time among the NV centers, with some requiring as little as 12 minutes, while others took up to 800 minutes to reach the stable PL regime. This variability in conversion time even at consistent laser powers suggests that the revival process is highly sensitive to the local conditions of each NV center, such as its proximity to the surface, the existing surface termination, and the density of additional nitrogen atoms in the vicinity of the NV center [18].
Fig. 8 (B,C) present the PL intensity, ODMR contrast, and SNR on the oxygen terminated and the converted surface. Notably, the NV's 1-4 are the same NV's across all figures. No significant change in PL was observed between the two surfaces following as shown in Fig. 8 (B).

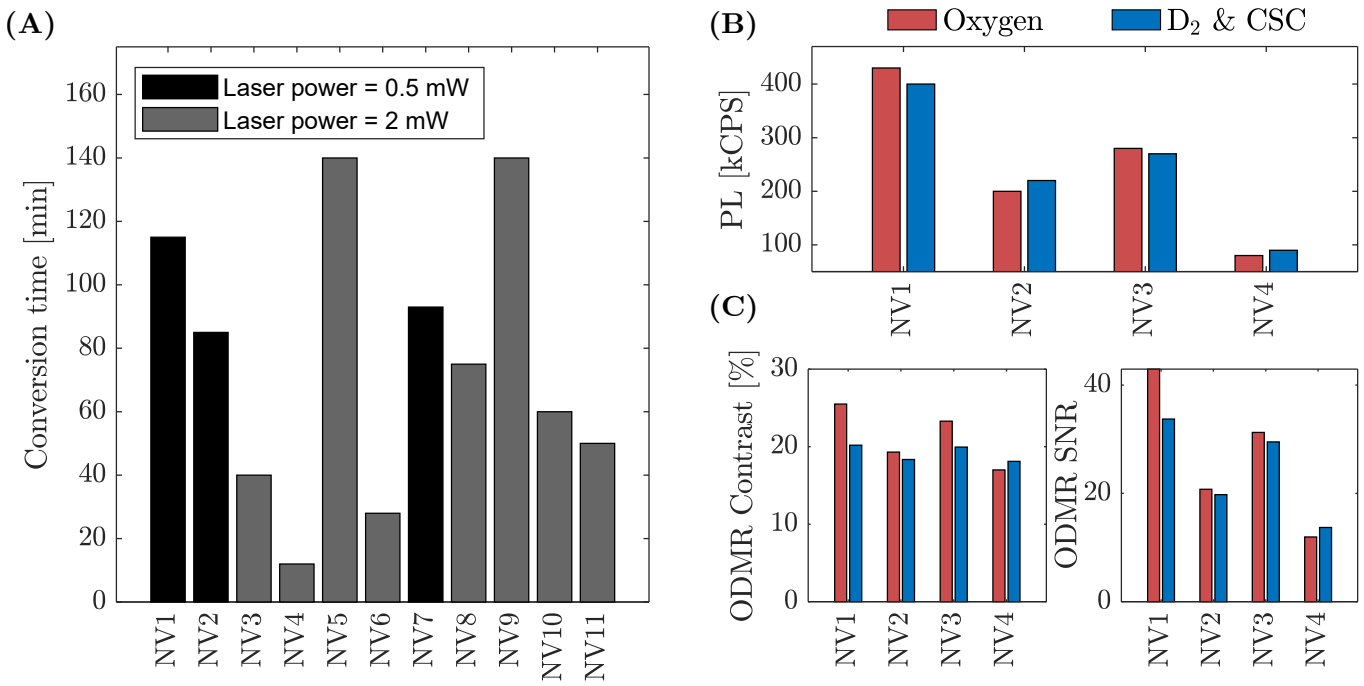

Figure 8: **(A)** Total duration and laser power used for the charge-state conversion process across different NV centers. The bars represent the total laser illumination time. The black and grey colors indicate the laser power applied during the process. **(B)** Comparison of PL intensity on oxygen terminated diamond (red) and after D_2 termination and successful charge-state conversion (blue). **(C)** ODMR contrast and SNR, on oxygen terminated diamond (red) and after D_2 termination and successful charge-state conversion (blue). Note that NV's 1-4 are the same NV's across all the figures in Fig. 8

The comparison of ODMR contrast and SNR before termination and after charge-state conversion, Fig. 8 (C), was performed using consistently calibrated MW power during ODMR measurements, enabling accurate assessment across the two surface terminations. Calibration was achieved by setting the MW power to produce a Rabi oscillation frequency of 3 MHz, establishing a standardized reference for evaluating contrast and SNR. The findings reveal enhanced contrast and SNR on the oxygen-terminated surface.

5 SNR Optimization In Spin-Lock NMR

5.1 Environmental Noise And Its Impact On Spin Relaxation

The spin system of the NV center is subject to environmental noise, which influences the NV spin's coherence time. Examples of environmental noise are random fluctuations in the surrounding electromagnetic fields, nuclear spin bath, and thermal vibrations, all of which interact with the NV center's spin state. These interactions lead to the decay of the spin system, which can be characterized by two distinct types of decay mechanisms: relaxation and dephasing.
The first type of decay is relaxation, referred to as a T_1 decay. Relaxation occurs along the spin quantization axis and arises from magnetic fluctuations at the transition frequency ω_0, where $\hbar\omega_0$ is the energy splitting of the ground state between the $|0\rangle$ and $|-1\rangle$ states, [10]. At room temperature, the relaxation time can extend into the millisecond range [21].
Dephasing, on the other hand, affects the spin components that are perpendicular to the quantization axis and arises from zero frequency noise as well as magnetic fluctuations at the transition frequency ω_0, [10]. This process leads to decoherence, which can severely limit the ability to maintain and manipulate the quantum state of the NV center. Dephasing is characterized by the timescale T_2^*, which is much shorter than T_1 on the order of microseconds [22]. Decoherence arises due to fluctuations in the local magnetic environment, which cause variations in the Zeeman splitting of the NV center's spin levels. These fluctuations result in phase errors and ultimately lead to decoherence of the spin state.
An important concept in understanding the impact of environmental noise on the NV center's spin coherence is the filter function [23], which describes how sensitive the spin is to different frequency components of the environmental noise. The noise itself is characterized by its spectral density, $S(\omega)$, which defines the distribution of noise power over frequency. The degree to which environmental noise influences dephasing during MW-based pulse sequences is determined by the overlap between the filter function $F(\omega)$ and the noise spectral density $S(\omega)$. Minimizing the overlap between $F(\omega)$ and $S(\omega)$ is key to extending the coherence time of the NV spin system and mitigating the effects of environmental noise during quantum operations.
In addition to mitigating unwanted noise, the filter function can also be used to selectively sense specific noise sources. This makes it possible to sense for example the Larmor frequency from nearby nuclear spins that precess in a magnetic field. This selective noise sensing is crucial in quantum sensing applications, where the objective is to isolate and detect a particular noise signature while suppressing other background noise.

5.2 Microwave-Based Spin Manipulation and Noise Protection

The spin states of nitrogen-vacancy (NV) centers can be coherently controlled through the application of transverse microwave (MW) fields. These fields serve as a crucial tool in quantum control, allowing for precise manipulation of spin states and mitigating environmental noise. This section offers an overview of MW-driven spin manipulation, with more in-depth discussion available e.g. in the work of Gerry and Knight [24].
We treat the NV spin system as an effective two-level system formed by the states $|0\rangle$ and $|-1\rangle$. The energy gap between these two states is given by $\omega_0 = D_{\text{gs}} - \gamma_{\text{NV}} B_z$, where D_{gs} represents the zero-field splitting, γ_{NV} is the gyromagnetic ratio, and B_z is the magnetic field along the NV axis. This energy gap sets the resonance frequency for microwave excitation. When a linearly polarized MW field is applied, it drives transitions between the $|0\rangle$ and $|-1\rangle$ states, resulting in coherent Rabi oscillations. For a microwave driving field detuned from resonance by a detuning δ, the resulting Rabi frequency is $\Omega = \sqrt{\delta^2 + \Omega_R^2}$.
The Bloch sphere provides an intuitive representation of the spin's quantum state and its evolution. On this sphere, the $|0\rangle$ and $|-1\rangle$ states are represented by the poles, while points on the surface represent superposition states. The effect of the MW field is visualized as a rotation of the spin vector within the Bloch sphere, which corresponds to an effective magnetic field in the rotating frame.
The orientation of the Rabi vector, which dictates the direction of the spin rotation, is controlled by the amplitude, phase, and detuning of the MW pulse. Mathematically, the components of the Rabi vector are

expressed as $(\mathrm{Re}(\Omega_R), -\mathrm{Im}(\Omega_R), \delta)$, where Ω_R is the complex Rabi frequency, and δ is the detuning. The MW pulse phase directly influences the direction of the Rabi vector in the xy-plane, allowing precise control over the spin dynamics by adjusting the phase.
Pulsing the resonant MW such that it performs exactly half a Rabi period, which corresponds to a full spin transition between the $|0\rangle$ and $|-1\rangle$ states, is called a π-pulse. On the Bloch sphere, such a π-pulse causes a rotation of the spin vector by 180°. Similarly, a $\pi/2$-pulse rotates the spin by half that angle on the Bloch sphere.

5.3 The Spin-Lock Sequence

MW driving is of particular interest to protect the NV spin system from environmental noise, specifically through techniques such as dynamical decoupling and the Spin-Lock protocol. In the Spin-Lock sequence, Fig. 9 (A), [25], after initial optical pumping into $|0\rangle$ Fig. 9 (B), the spin system is brought into a superposition state on the equatorial plane of the Bloch sphere via a $\pi/2$ pulse, Fig. 9 (C). This first pulse can be done around an arbitrary Rabi vector, which defines the Bloch sphere's axes. We here define this axis as the x axis. Following this, a second MW pulse is applied along the y axis of the Bloch sphere aligned with the spin vector, Fig. 9 (D). This is achieved by a 90° phase shift in the MW pulse. Since the spin vector rotates around any applied Rabi vector, this alignment "locks" the spin vector, hence the name Spin-Lock. This second pulse is from here on referred to as the "Spin-Lock" pulse. During this "locking", the orientation of the Rabi vector can be treated as the new quantization axis. This new quantization axis lies on the equatorial plane of the Bloch sphere. Along this axis, the spin states are no longer described by the original Eigenstates $|0\rangle$ and $|-1\rangle$, but by so-called dressed states, here $|+\rangle$ and $|-\rangle$, which now represent the Eigenstates of the system in the presence of the MW driving field, as displayed in Fig. 9 (D-F).
The Spin-Lock pulse is followed by another $\pi/2$ pulse around the x axis Fig. 9 (E), projecting the spin vector back to the z axis of the Bloch sphere, allowing for optical readout of the spin state, Fig. 9 (F). This flip can be a $+\pi/2$ pulse, projecting the spin vector onto the $|-1\rangle$ state, or $-\pi/2$ pulse, projecting the spin vector onto the $|0\rangle$ state. Measurements in this thesis consist of both such $\pm\pi/2$ pulses from which the difference in PL is taken. This helps with averaging out global PL drifts, for example due to temperature fluctuations. The decay of these dressed states is characterized by a relaxation constant denoted as $T_{1\rho}$. This timescale describes the relaxation of the spin system along the new quantization axis, as the dressed states decay towards the center of the Bloch sphere. The $T_{1\rho}$ time thus quantifies the spin relaxation in this locked configuration, analogous to the T_1 relaxation in the original basis, offering enhanced protection against environmental noise. This resilience arises because $T_{1\rho}$ is primarily sensitive to magnetic fluctuations at specific frequencies: the NV center's transition frequency ω_0 where $\hbar\omega_0$ represents the energy splitting between the m_S $|0\rangle$ and m_S $|-1\rangle$ spin states of the NV center and the Spin-Lock field's Rabi frequency Ω_0 [10]. Notably, typical environmental noise sources are largely characterized by low-frequency fluctuations, which do not align with ω_0 or Ω_R and therefore exert minimal impact on $T_{1\rho}$. This frequency selectivity reduces the NV center's susceptibility to noise that would otherwise limit coherence time.

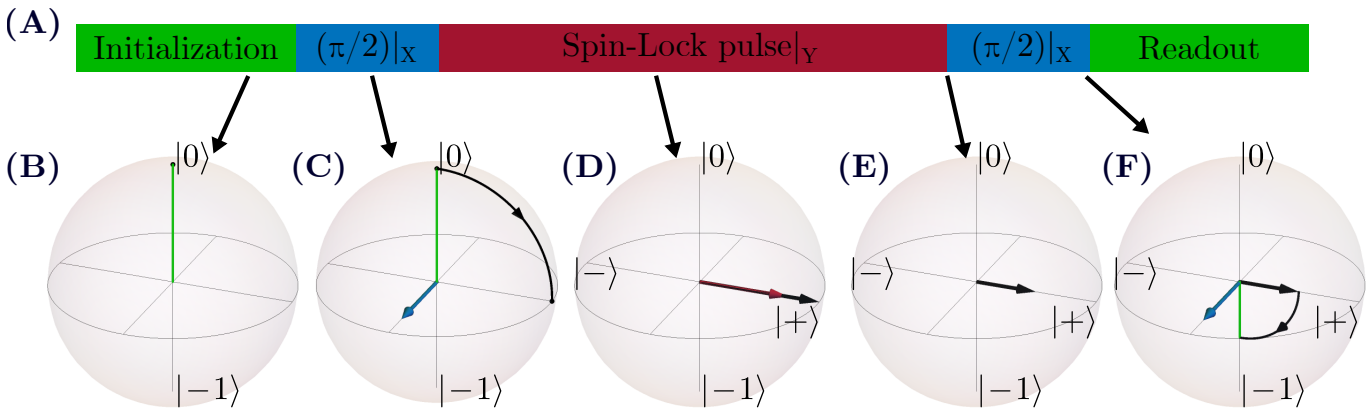

Figure 9: **(A)** Schematic of the Spin-Lock sequence used in the experiment. The initialization and readout are performed with a green 515 nm laser. After initialization and before readout a $\pi/2$ pulse along the X-axis is performed (blue part in **(A)**), followed by a Spin-Lock pulse along the Y-axis (red). **(B)** Bloch sphere representation the initialization into $|0\rangle$. **(C)** The intitial $+\pi/2$ pulse. The blue vector represents the Rabi vector around which the spin vector (black) rotates. **(D)** The red Spin-Lock pulse locks the spin vector (black). **(F)** The spin system decay's with the time constant $T_{1\rho}$ during the Spin-Lock pulse. **(F)** The second $+\pi/2$ pulse with Rabi vector in blue as in **(C)**, mapping the spin state back to the Z-axis of the Bloch sphere.

Nuclear spins in an external magnetic field precess at a frequency known as the Larmor frequency that for protons is given by $\omega_L = \gamma_H \cdot B$, where γ_H is the gyromagnetic ratio of the proton and B is the strength of the external magnetic field. This precession creates an oscillating magnetic field at the Larmor frequency which manifests as magnetic noise at the Larmor frequency in the noise spectral density. For protons the Larmor frequency at the ESLAC (512G) is about 2.18 MHz [26]. By sweeping the amplitude Ω_R of the Spin-Lock pulse over a range of frequencies, the system's noise sensitivity is swept across the same spectral window. Therefore, when the Spin-Lock field strength Ω_R is equal or close to the Larmor frequency ω_L of the nuclear spin bath, the NV spin experiences increased noise at this specific Spin-Lock amplitude due to the resonant coupling to the precessing hydrogen nuclei, which leads to a decreased $T_{1\rho}$ relaxation time. This reduction in $T_{1\rho}$ at the resonance condition manifests as a dip in the spin readout signal after the Spin-Lock sequence allowing the NMR signal from the hydrogen nuclear spins to be detected. A typical Spin-Lock NMR spectrum is shown in Fig. 10 (A).

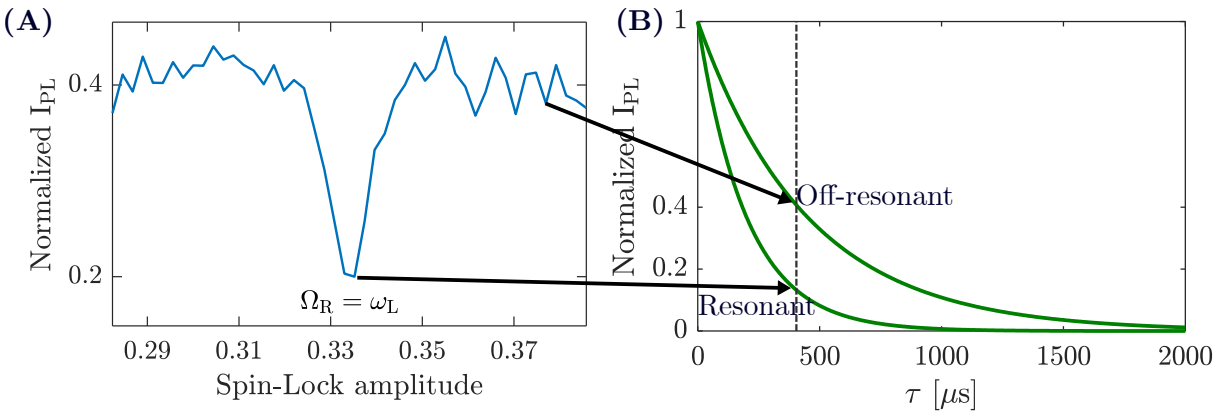

Figure 10: **(A)** Typical Spin-Lock NMR spectrum showing the NMR feature at the Larmor frequency of hydrogen ω_L. **(B)** Simulated $T_{1\rho}$ relaxation curves, once off-resonant and once resonant $\Omega_R = \omega_L$.

In this thesis, the key parameters used to describe such NMR spectra are the contrast, the STD, and the SNR. Contrast is defined as the difference between the PL at resonance and the baseline, divided by the

baseline PL. The STD is a measure of the noise of the data. It is calculated as the standard deviation of the baseline. The SNR is defined as the ratio of the contrast and the STD and determines the sensitivity of the NMR measurement. Therefore, optimizing for SNR in a Spin-Lock measurement is crucial and is the topic of Sec.5.4

5.4 Optimal Duration Of Spin-Lock Pulse Via Noise-Level Simulations

In a Spin-Lock NMR measurement as described above, the free parameter to be set is the duration of the Spin-Lock pulse, denoted as τ. This parameter plays a critical role in optimizing the SNR but also determines what NMR frequency resolution can be achieved at best due to Fourier limitations. A typical Spin-Lock NMR measurement is performed at a fixed τ, as indicated by the grey dotted line in Fig. 10 (B). At this chosen duration, the amplitude of the Spin-Lock pulse is swept, creating the Spin-Lock spectra. Similarly, $T_{1\rho}$ decay curves can be measured by choosing a fixed amplitude Ω_R for the Spin-Lock pulse. This allows for the measurement of $T_{1\rho}$ decay curves at different amplitudes: one corresponding to the off-resonant condition, at a NMR frequency far detuned from the hydrogen Larmor frequency ω_L, and another at the resonant amplitude, where $\Omega_R = \omega_L$. Based on the preceding discussion, the decay time for the resonant condition, $T_{1\rho,\text{resonant}}$, is expexted to be shorter than the off-resonant decay time, $T_{1\rho,\text{off-resonant}}$. A simulated example of such decay curves is shown in Fig. 10 (B).
As demonstrated by the subsequent equations, the contrast between the resonant and off-resonant signals increases with the duration τ. However, extending τ also increases the total sequence duration, which reduces the number of repetitions that can be performed within a fixed time window. This leads to an increase in noise per unit time. Simulations have been carried out to model the trade-off between signal contrast and noise, with the goal of determining the optimal Spin-Lock pulse duration τ.
The decay curves in Fig. 10 (A) are described by a simple exponential decay:

$$\Delta_{\text{PL}} \cdot \exp\left(-\frac{\tau}{T_{1\rho}}\right),$$

where Δ_{PL} is the PL difference between $|0\rangle$ and $|-1\rangle$ and $T_{1\rho}$ is either the off-resonant or the resonant decay constant.
The contrast $\mathrm{C}(\tau)$ is defined as the difference in PL between the two decay curves at the specific τ, normalized by the background, Eq. (2).

$$\mathrm{C}(\tau) = \frac{\exp\left(-\frac{\tau}{T_{1\rho,\text{resonant}}}\right) - \exp\left(-\frac{\tau}{T_{1\rho,\text{off-resonant}}}\right)}{\exp\left(-\frac{\tau}{T_{1\rho,\text{off-resonant}}}\right)} \tag{2}$$

The noise in the measurement is modeled as a Gaussian random variable with 0 mean and variance σ: $X \sim \mathcal{N}(0, \sigma)$. Since the PL signal is derived by subtracting the results from the $-\pi/2$ and $+\pi/2$ measurements—both of which contain noise—this leads to the subtraction of two independent Gaussian random variables. The result is a new Gaussian distribution with variance $\sqrt{2} \cdot \sigma$, i.e., $X \sim \mathcal{N}(0, \sqrt{2} \cdot \sigma)$ [27].
To account for the additional noise introduced by longer pulse durations, an extra multiplicative factor of $\sqrt{\tau}$ is applied in the noise model. This factor arises from the relationship between the pulse duration τ and the STD of the signal. Specifically, the SNR increases with the square root of the number of repetitions, where SNR = Contrast/STD. As a result, the STD scales inversely with the square root of the repetitions, or STD $\propto 1/\sqrt{\text{reps}}$ and since the number of repetitions is inversely proportional to the pulse duration (i.e., reps $\propto 1/\tau$), it follows that the STD scales with $\sqrt{\tau}$. This additional $\sqrt{\tau}$ factor thus adjusts the noise model to account for the increased noise from fewer repetitions at longer pulse durations, providing a more accurate representation of measurement noise. This leads to the following noise model: $X \sim \mathcal{N}(0, \sqrt{2} \cdot \sqrt{\tau} \cdot \sigma)$. The STD is then given by Eq. (3):

$$\begin{aligned} \mathrm{STD}(\tau) &= \mathrm{std}\left(\frac{\mathcal{N}(0, \sqrt{2}\cdot\sqrt{\tau}\cdot\sigma)}{\Delta_{PL}\cdot\exp\left(-\frac{\tau}{T_{1\rho,\text{off-resonant}}}\right)}\right) \\ &= \frac{\sqrt{2}\cdot\sqrt{\tau}\cdot\sigma}{\Delta_{PL}\cdot\exp\left(-\frac{\tau}{T_{1\rho,\text{off-resonant}}}\right)} \end{aligned} \tag{3}$$

The SNR, given by $\frac{\mathrm{C}(\tau)}{\mathrm{STD}(\tau)}$ is determined by taking the ratio of the contrast Eq. (2) and the STD Eq. (3):

$$\mathrm{SNR}(\tau) = \frac{\Delta_{PL}\cdot\left(\exp\left(-\frac{\tau}{T_{1\rho,\text{off-resonant}}}\right) - \exp\left(-\frac{\tau}{T_{1\rho,\text{resonant}}}\right)\right)}{\sqrt{2}\cdot\sqrt{\tau}\cdot\sigma} \tag{4}$$

Calculating the optimal duration for the Spin-Lock pulse (i.e. the value of tau that maximises the SNR) with Eq. (4) requires measuring the values $\Delta_{PL} = 35$ kCPS, $T_{1\rho,\text{off-resonant}} = 801\mu\text{s}\pm44\mu\text{s}$ and $T_{1\rho,\text{resonant}} = 349\mu\text{s}\pm34\mu\text{s}$. The optimal duration for a Spin-Lock NMR measurement in this case is τ=248µs.
Using the values for Δ_{PL}, $T_{1\rho,\text{off-resonant}}$ and $T_{1\rho,\text{resonant}}$, experimental data from Spin-Lock NMR's were fitted to the analytical solution for the STD, Eq. (3), to obtain the intrinsic noise variance $\sigma = 0.065\pm0.004$. This σ is essentially a scaling factor for the STD that depends on the intrinsic noise level of the specific NV/Pillar that is investigated. Determining σ through a fitting routine is necessary to plot the SNR(τ) analytical solution in Eq. (4). In Fig. 11 the analytical solutions for the STD, contrast and SNR as a function of τ are shown (black lines). The fit uncertainties from the $T_{1\rho}$ measurements are displayed as the grey areas and give an error for the analytical solutions. The red dots are data points from Spin-Lock measurements with error bars which come from fit uncertainties. The data aligns closely with the model, confirming its credibility.

In summary, the analysis presented in this chapter demonstrates the delicate balance between increasing the signal contrast and managing noise levels, both of which are influenced by the chosen Spin-Lock pulse duration. Through an analytical model for the STD, contrast and SNR, the optimal duration for the Spin-Lock pulse can be determined by experimentally measuring Δ_{PL}, $T_{1\rho,\text{off-resonant}}$ and $T_{1\rho,\text{resonant}}$. The consistency between the experimental data and the theoretical predictions highlight the credibility of the model and the insights gained from this work guide the practical implementation of Spin-Lock experiments.

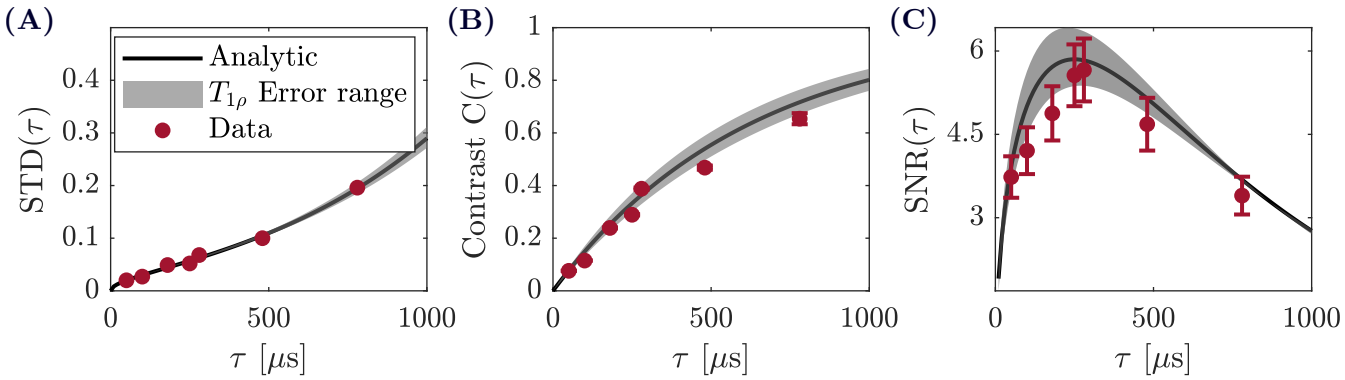

Figure 11: Analytic solutions for the STD **(A)**, contrast **(B)** and SNR **(C)** as a function of τ, black lines. The grey areas represent the error range of the analytical solutions from fit uncertainties in the $T_{1\rho}$ measurements. The red dots show data points from Spin-Lock NMR measurements with error-bars from fit uncertainties.

6 Spin-Lock NMR On Different Diamond Surfaces

In our investigation of an oxygen-terminated diamond surface, that is prepared using a tri-acid cleaning process, we observed an intriguing and unexpected hydrogen signal in Spin-Lock NMR measurements. This observation was particularly notable as the signal was detected on a freshly tri-acid cleaned diamond sample with clean surface, that's without the presence of any external contaminants, oils, or substances known to generate such hydrogen signals. The fact that Spin-Lock NMR still shows a proton feature suggests a significant interaction involving hydrogen, but the origin of such hydrogen remains uncertain.
A possible explanation for this is the presence of hydrogen atoms on the diamond surface, either as part of direct hydrogen bonds or within hydroxyl (OH) groups formed during or after the tri-acid cleaning process. However, it is challenging to pinpoint whether the hydrogen atoms are strictly surface-bound or embedded within the uppermost layers of the diamond.

Following the detection of a hydrogen NMR signal on the oxygen-terminated diamond, deuterium (D_2) termination of the diamond is pursued to replace any potential surface-bound hydrogen species with D_2, which is not supposed to yield any signal at the proton NMR frequency. However, D_2 termination of the diamond surface results in an unfavorable surface termination for the negatively charged NV^- state, yielding primarily neutral NV^0 centers, similar to what is observed with hydrogen termination [7]. In order to restore the NV^- charge state, a charge-state conversion process is necessary, which is successfully achieved through laser illumination, as described in Chapter 4.
Following the NV^- charge-state conversion, the Spin-Lock NMR measurements have been repeated to assess possible changes in the hydrogen NMR signal. The hydrogen NMR signal persisted, supporting the hypothesis presented in Section 4.1, which suggests that the initial D_2 termination gets gradually replaced by a mixture of mostly hydroxyl (OH) groups, and C-O-C bonds as a result of surface oxidation during the NV charge-state conversion process.
Comparing the two Spin-Lock NMR spectra, done on oxygen terminated diamond Fig. 12 (A) and on the covnerted surface Fig. 12 (B), provides further insights into the hydrogen NMR signal that we will discuss in the following.

6.1 Comparison Of Spin-Lock NMR Spectra On Oxygen and D_2 Terminated Diamond

The results of the Spin-Lock NMR measurements on the oxygen and the converted surface are presented in Fig. 12. Both spectra were recorded under identical total measurement times, but with different Spin-Lock evolution times of τ_{oxygen}=215µs and $\tau_{\text{converted}}$=280µs corresponding to their respective optimal duration. Notably, the SNR on the D_2-terminated diamond surface improved by a factor of 1.8 on the converted surface. This increase in SNR can be attributed to one of two factors: either an enhancement in the hydrogen NMR signal strength due to a higher proton density (leading to a shortened $T_{1\rho,\text{resonant}}$) on the surface or a reduction in background noise (leading to a prolonged $T_{1\rho,\text{off-resonant}}$) caused by the change in surface chemistry from oxygen-terminated to D_2-terminated and charge-state-converted diamond.
Interestingly, the off-resonant decay time, $T_{1\rho,\text{off-resonant}}$, on the converted surface is nearly twice that of the oxygen-terminated surface (see grey boxes in Fig. 12 (A)), suggesting a less noisy environment which results in slower NV spin system decay on the D_2-terminated surface. A reduction in background noise would naturally lead to an improved SNR, even if the hydrogen signal strength remained constant.
To better quantify the contribution of the hydrogen NMR signal, one can calculate its impact on the resonant decay time $T_{1\rho,\text{resonant}}$. The increased decay rate at the resonant frequency can be interpreted as an additional decay component, $T_{1\rho,\text{hydrogen}}$, which adds to the background decay rate, $T_{1\rho,\text{off-resonant}}$, as shown in Eq. (5).

$$\frac{1}{T_{1\rho,\text{resonant}}} = \frac{1}{T_{1\rho,\text{off-resonant}}} + \frac{1}{T_{1\rho,\text{hydrogen}}} \tag{5}$$

With this, the contribution of the hydrogen signal to the overall resonant decay can be computed (Eq. (6)), providing a clearer understanding of the NMR signal's strength.

$$T_{1\rho,\text{hydrogen}} = \left(\frac{1}{T_{1\rho,\text{resonant}}} - \frac{1}{T_{1\rho,\text{off-resonant}}} \right)^{-1} \tag{6}$$

The results, shown in the inset of Fig. 12 (A), reveal that the hydrogen signal's contribution to the resonant decay rate on the converted surface is about four times greater than on the oxygen-terminated diamond. This suggests a significant increase in the strength of the hydrogen NMR signal after D_2 termination. This enhancement in signal strength is most likely attributed to an increase in the density of hydrogen species on the diamond surface following D_2 termination and charge-state conversion. After D_2 termination and charge-state conversion, the diamond surface demonstrates a longer $T1\rho$, off-res relaxation time, while simultaneously showing a stronger proton signal, as evidenced by a shorter $T_{1\rho,\text{hydrogen}}$, suggesting that the introduced hydrogen is not related with a source of decoherence noise. One possible explanation is that this hydrogen is covalently bonded to the diamond surface, leading to a well-defined interaction that strengthens the NMR signal without adversely affecting coherence properties.

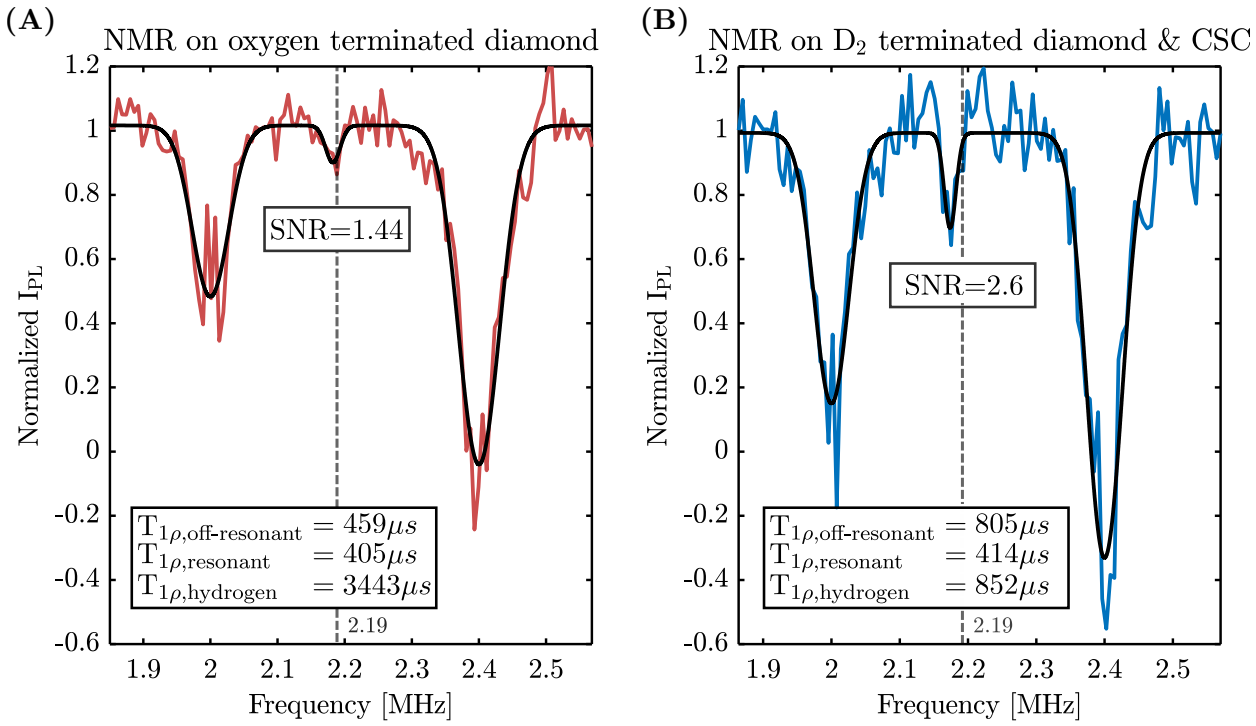

Figure 12: Data of Spin-Lock NMR measurements on the same pillar with **(A)** an oxygen terminated surface and **(B)** a D_2 terminated surface after successful charge-state conversion (converted surface). The data is normalized to the background PL level. The respective left and right Gaussian dips correspond to two calibration signals, positioned at 2 MHz and 2.4 MHz while the middle dip corresponds to the hydrogen NMR signal. The dashed line at 2.19 MHz indicates the theoretical value of the Larmor frequency based on the magnetic field determined by an ODMR measurement. The measured hydrogen NMR feature is slightly off from the calculated theoretical value.

Both spectra in Fig. 12 (A) also display the presence of two calibration signals at 2 MHz and 2.4 MHz, which were used to calibrate the frequency axis. It is important to note that the calibration signal at 2.4 MHz

shows a contrast greater than 100%, a phenomenon attributed to the coherent nature of the signal. This calibration signal actively drives Rabi oscillations between the dressed states of the system ($|+\rangle$ and $|-\rangle$, as discussed in Section 5.3), achieving full population transfer at specific τ durations, thereby producing a contrast above 100%.

Finally, both NMR spectra exhibit a slight offset of the hydrogen NMR signal from the expected position of 2.19 MHz, despite accurate calibration with the calibration signals. This consistent shift, observed across multiple experiments, remains unexplained. One potential cause are fitting errors in the calibration signal positions, which may propagate along the frequency axis. Another possibility is strain within the diamond lattice, which could result in a shift in the zero-field splitting of the NV, leading to a miscalculation of the magnetic field with an ODMR measurement. This would, in turn, cause a shift in the theoretical position of the hydrogen signal. This could be confirmed by detecting both ODMR resonance dips of the NV center. However, due to equipment limitations, measurement of the second ODMR dip was not feasible in this study.

Additionally, DC noise affecting the proton spins might contribute to the frequency shift, as residual DC fields could perturb the local environment of the protons and would act as a constant offset in the magnetic field. It is also possible that a combination of factors is responsible for the observed discrepancy, warranting further investigation to fully understand the underlying causes.

7 Summary

This thesis investigates the hydrogen NMR signal detected on oxygen-terminated diamond surfaces, attributed to surface-bound hydrogen species. To further explore the nature of this signal, the surface was D_2 terminated and subsequent charge-state converted. Spin-Lock NMR measurements were performed both on the oxygen terminated diamond and after D_2 termination and subsequent charge-state conversion on the same NV center, enabling a direct comparison of the hydrogen signal between these two surfaces.
To facilitate these measurements, the first part of this thesis focuses on the charge-state conversion of NV centers in diamond after D_2 termination. During the charge-state conversion process, the D_2 termination is gradually replaced by a mixture of oxygen, hydroxyl groups, and other species. This alteration in surface chemistry drives the transition from the neutral NV^0 state to the negatively charged NV^- state, restoring the NV's sensing capability. Notably, the emitted PL peaked throughout the restoration process when laser powers in the range of 0.5 mW to 2 mW were applied. At this PL peak, we expect the ratio of NV^- to NV^0 to be the highest, however, ODMR contrast only becomes significant once the PL drops to a stable level, suggesting that the PL peak reflects background contributions rather than the highest NV^- to NV^0 ratio. The high-power laser could attract "dirt" from the environment to the diamond surface, which are then gradually photo-bleached, causing an initial PL increase followed by a reduction. A spectral analysis was conducted throughout the charge-state conversion process. Interestingly, the PL continuously increased until saturation, possibly due to lower laser power (200 µW) reducing surface contamination. The ODMR contrast showed a gradual rise, attributed to more measurement repetitions revealing low-contrast features. PL spectra were used to quantify the contributions of NV^0 and NV^- by fitting each spectrum as a superposition of the reference NV^0 and NV^- spectra, revealing a progressive conversion from NV^0 to NV^-.

The oxygen-terminated surface and the converted surface after D_2 termination and charge-state conversion were compared in terms of ODMR contrast. Under the same calibrated MW power conditions between the two surfaces we observe superior contrast and SNR on the oxygen terminated surface.

The second part of this thesis investigates the hydrogen NMR signal detected on both these surfaces. Spin-Lock NMR measurements were performed on the same NV center both on oxygen terminated diamond and after the D_2 termination and successful charge-state conversion (converted surface). We report an off-resonant decay time ($T_{1\rho}$) on the D_2-terminated surface of nearly twice as long as that on the oxygen-terminated surface, supporting the conclusion of reduced background noise on the D_2-terminated surface. The resonant relaxation time attributed to the hydrogen spins $T_{1\rho,hydrogen}$ decreased by a factor of 4 on the converted surface, indicating that more hydrogen species appear on the surface due to alterations occurring during the charge-state conversion process. This leads to improved conditions for detecting hydrogen NMR signals using NV centers in diamond. These measurements were conducted thus far on a single NV center and further investigations across multiple NV centers are necessary to confirm and generalize these findings.

8 Outlook

This thesis raises several open questions and challenges that warrant further investigation. One puzzling observation is the appearance of ODMR contrast only at the PL plateau during the charge-state conversion process (Fig. 4 (C)), and not at the PL peak, as would be expected since the NV^- charge state is the brightest. A potential explanation for this behavior is that the observed PL peak may result from background PL contributions due to "dirt" attracted to the diamond surface by high-power laser illumination during the conversion process. Continued laser exposure can lead to photo-bleaching of these contaminants, causing a reduction in PL intensity and stabilization at the plateau. Spectral analysis measurements conducted at lower laser power (200 µW) showed a continuous increase in PL until saturation, without the distinct peak and decline seen at higher powers. This suggests that reducing laser power may limit surface contaminant accumulation, eliminating the characteristic PL peak behavior. Further studies should investigate how varying laser power influences PL dynamics and surface interactions during the charge-state conversion process.

Another key focus of this work was the investigation of the hydrogen signal using Spin-Lock NMR measurements. The origin of this hydrogen signal is hypothesized to come from surface-bound hydrogen species, presumably in the form of hydroxyl (OH) groups formed during the charge-state conversion process. Notably, the hydrogen NMR signal increased in strength on the converted surface compared to the oxygen-terminated surface, suggesting an increased hydrogen density on the converted surface. Further investigation could involve the measurement of deuterium NMR signals, allowing a more detailed understanding of the charge-state conversion process and how it alters the surface chemistry and also realizing a pure oxygen termination to remove any surface bound hydrogen. Additionally, the observed shift in the Spin-Lock resonance position of the hydrogen signal requires further exploration, as it may provide insight into the local magnetic environment.

Declaration of Scientific Integrity

Hiermit erkläre ich, dass ich ausser der angegebenen Literatur keine weiteren Hilfsmittel benutzt habe und dass mir bei der Zusammenstellung des Materials und der Abfassung der Arbeit von niemandem geholfen wurde. Ich bestätige hiermit, dass ich vertraut bin mit den Regelungen zum Plagiat der «Ordnung der Philosophisch-Historischen Fakultät der Universität Basel für das Masterstudium vom 25. Oktober 2018» (§25) und die Regeln der wissenschaftlichen Integrität gewissenhaft befolgt habe. Die vorliegende Arbeit ist ausserdem weder ganz noch teilweise an einer anderen Fakultät oder Universität zur Begutachtung eingereicht und/oder als Studienleistung z.B. in Form von Kreditpunkten verbucht worden. Ich bezeuge mit meiner Unterschrift, dass meine Angaben über die bei der Erstellung meiner Masterarbeit benutzten Hilfsmittel, über die mir zuteil gewordene Hilfe sowie über die frühere Begutachtung meiner Masterarbeit in jeder Hinsicht der Wahrheit entsprechen und vollständig sind.

Basel, November 12, 2024
Patrik Tognina

References

[1] M. W. Doherty, N. B. Manson, P. Delaney, F. Jelezko, J. Wrachtrup, and L. C. Hollenberg, *The nitrogen-vacancy colour centre in diamond*, Physics Reports **528**, 1, the nitrogen-vacancy colour centre in diamond (2013).

[2] N. Bar-Gill, L. Pham, A. Jarmola, D. Budker, and R. Walsworth, *Solid-state electronic spin coherence time approaching one second*, Nature Communications **4** (2013).

[3] R. Schirhagl, K. Chang, M. Loretz, and C. L. Degen, *Nitrogen-vacancy centers in diamond: Nanoscale sensors for physics and biology*, Annual Review of Physical Chemistry **65**, 83 (2014).

[4] P. Maletinsky, S. Hong, M. Grinolds, B. Hausmann, M. Lukin, R. Walsworth, M. Loncar, and A. Yacoby, *A robust scanning diamond sensor for nanoscale imaging with single nitrogen-vacancy centres*, Nature nanotechnology **7**, 320 (2012).

[5] A. Boretti, L. Rosa, J. Blackledge, and S. Castelletto, *Nitrogen-vacancy centers in diamond for nanoscale magnetic resonance imaging applications*, Beilstein Journal of Nanotechnology **10**, 2128 (2019).

[6] L. Rondin, J.-P. Tetienne, T. Hingant, J.-F. Roch, P. Maletinsky, and V. Jacques, *Magnetometry with nitrogen-vacancy defects in diamond*, Reports on Progress in Physics **77**, 056503 (2014).

[7] M. V. Hauf, B. Grotz, B. Naydenov, M. Dankerl, S. Pezzagna, J. Meijer, F. Jelezko, J. Wrachtrup, M. Stutzmann, F. Reinhard, and J. A. Garrido, *Chemical control of the charge state of nitrogen-vacancy centers in diamond*, Phys. Rev. B **83**, 081304 (2011).

[8] J. A. Zuber and P. Maletinsky, *Optical spectroscopy of shallow silicon vacancy centers in diamond nanostructures*, npj Quantum Inf p. 104 (2024).

[9] Y. Ting and D. Williams, *Nuclear gyromagnetic ratios. iv*, Phys. Rev. **89**, 595 (1953).

[10] BeatBuergler, *Depth determination of single nv centers via spin-locked hydrogen sensing*, accessed: 25 September 2024 (2020).

[11] M. Steiner, P. Neumann, J. Beck, F. Jelezko, and J. Wrachtrup, *Universal enhancement of the optical readout fidelity of single electron spins at nitrogen-vacancy centers in diamond*, Phys. Rev. B **81**, 035205 (2010).

[12] S. Felton, A. M. Edmonds, M. E. Newton, P. M. Martineau, D. Fisher, D. J. Twitchen, and J. M. Baker, *Hyperfine interaction in the ground state of the negatively charged nitrogen vacancy center in diamond*, Phys. Rev. B **79**, 075203 (2009).

[13] M. Steiner, P. Neumann, J. Beck, F. Jelezko, and J. Wrachtrup, *Universal enhancement of the optical readout fidelity of single electron spins at nitrogen-vacancy centers in diamond*, Phys. Rev. B **81**, 035205 (2010).

[14] B. Bürgler, T. F. Sjolander, O. Brinza, A. Tallaire, J. Achard, and P. Maletinsky, *All-optical nuclear quantum sensing using nitrogen-vacancy centers in diamond*, npj Quantum Information **9** (2023).

[15] N. Hedrich, D. Rohner, M. Batzer, P. Maletinsky, and B. J. Shields, *Parabolic diamond scanning probes for single-spin magnetic field imaging*, Phys. Rev. Appl. **14**, 064007 (2020).

[16] B. A. T. F. J.-P. C. Moloud Kaviani, Peter Deák and A. Gali, *Proper surface termination for luminescent near-surface nv centers in diamond*, Nano Lett. **14**, 47724777 (2014).

[17] M. V. Hauf, B. Grotz, B. Naydenov, M. Dankerl, S. Pezzagna, J. Meijer, F. Jelezko, J. Wrachtrup, M. Stutzmann, F. Reinhard, and J. A. Garrido, *Chemical control of the charge state of nitrogen-vacancy centers in diamond*, Phys. Rev. B **83**, 081304 (2011).

[18] A. T. Collins, *The fermi level in diamond*, Journal of Physics: Condensed Matter **14**, 3743 (2002).

[19] L. V. H. Rodgers, S. T. Nguyen, J. H. Cox, K. Zervas, Z. Yuan, S. Sangtawesin, A. Stacey, C. Jaye, C. Weiland, A. Pershin, A. Gali, L. Thomsen, S. A. Meynell, L. B. Hughes, A. C. B. Jayich, X. Gui, R. J. Cava, R. R. Knowles, and N. P. de Leon, *Diamond surface functionalization via visible light–driven c–h activation for nanoscale quantum sensing*, Proceedings of the National Academy of Sciences **121**, e2316032121 (2024).

[20] S. Parthasarathy, M. Joos, L. B. Hughes, S. A. Meynell, T. A. Morrison, J. D. Risner-Jamtgaard, D. M. Weld, K. Mukherjee, and A. C. B. Jayich, *Role of oxygen in laser induced contamination at diamond-vacuum interfaces* (2024), 2401.06942.

[21] T. Rosskopf, A. Dussaux, K. Ohashi, M. Loretz, R. Schirhagl, H. Watanabe, S. Shikata, K. M. Itoh, and C. L. Degen, *Investigation of surface magnetic noise by shallow spins in diamond*, Phys. Rev. Lett. **112**, 147602 (2014).

[22] J. R. Maze, A. Dréau, V. Waselowski, H. Duarte, J.-F. Roch, and V. Jacques, *Free induction decay of single spins in diamond*, New Journal of Physics **14**, 103041 (2012).

[23] J. Du, F. Shi, X. Kong, F. Jelezko, and J. Wrachtrup, *Single-molecule scale magnetic resonance spectroscopy using quantum diamond sensors*, Rev. Mod. Phys. **96**, 025001 (2024).

[24] P. K. C. Gerry and P. Knight, *Introductory quantum optics*, Cambridge University Press (2005).

[25] C. Slichter, *Principles of Magnetic Resonance*, , Harper's physics series (Harper & Row) (1980).

[26] H. A. Thomas, R. L. Driscoll, and J. A. Hipple, *Measurement of the proton moment in absolute units*, Phys. Rev. **78**, 787 (1950).

[27] *Wolframalpha*, https://mathworld.wolfram.com/NormalDifferenceDistribution.html, accessed: 22 September 2024 (2024).